RESEARCH ARTICLE

ADVANCED MATERIALS INTERFACES
Open Access
www.advmatinterfaces.de

The Role of Dynamic Solvent Swelling in Electrochemical Doping of Semiconducting Polymers

Charlene Z. Salamat, Bintao Hu, Nesibe Akmanşen-Kalayci, Germany la Diaz De la Cruz, Linnea Shu, Alex Leon Ruiz, Quynh M. Duong, Barry C. Thompson, Sri R. Narayan, Benjamin J. Schwartz, Sarah H. Tolbert, and Bruce S. Dunn**

Semiconducting polymers are of interest due to their solution processibility and broad electronic applications. Electrochemistry allows these wide bandgap semiconductors to be converted to conducting polymers by doping such polymers at various potentials. When polymers are *p*-doped to improve their conductivity via electrochemical oxidation, various positively-charged carriers are created, including polarons (singly-charged) and bipolarons (doubly-charged). Carrier creation is accompanied by anion intercalation from the electrolyte for charge balance, and this insertion requires ion mobility. In this work, poly(3-hexylthiophene) (P3HT) with different regioregularities is used to understand the relationship between solvent swelling, which affects anion intercalation, and electrochemical doping. Cyclic voltammetry, optical absorption spectroscopy, and grazing incidence wide-angle X-ray scattering (GIWAXS) measurements are used to correlate the doping level with structural changes. In situ electrochemical quartz crystal microbalance (EQCM) measurements are used to quantify the swelling of the polymers dynamically during electrochemical cycling. Lastly, in situ conductivity measurements are done to measure the effect of swelling on the ionic and electronic conductivity. The results indicate that solvent swelling is required for bipolaron formation, and that swelling facilitates both the small structural changes need for polaron formation and the disordering required for bipolaron formation.

1. Introduction

Semiconducting polymers are of significant interest due to their potential utilization in energy storage and electronic devices.[1–6] These materials are wide bandgap semiconductors, and thus, at room temperature, have little to no charge carriers. Doping enables the addition of charge carriers by oxidation (*p*-type)[7,8] or reduction (*n*-type)[9,10] of the polymer backbone. This can be accomplished by chemical doping, where for *p*-doping a small molecule oxidizer undergoes charge transfer with the conjugated polymer to create a charge carrier on the polymer backbone and a charge-balancing counterion.[11–13] Another method to add charge carriers is by applying an electric potential to electrochemically dope semiconducting polymers; here, an anion from the electrolyte enters the polymer matrix for charge compensation.[14–16] While chemical doping requires the use of dopants with different oxidizing strengths to tune doping levels, electrochemical doping allows for doping to varying, controlled levels using a single electrolyte, simplifying our understanding of the system.[17–20]

Electrochemical methods can give information about the energetics of doping in semiconducting polymers. For example, cyclic voltammetry (CV), which records the current response as the electrode potential is linearly ramped, is commonly used to observe oxidation and reduction energies

---

C. Z. Salamat, N. Akmanşen-Kalayci, L. Shu, A. Leon Ruiz, Q. M. Duong,
B. J. Schwartz, S. H. Tolbert
Department of Chemistry and Biochemistry
University of California, Los Angeles
Los Angeles, CA 90095-1569, USA
E-mail: tolbert@chem.ucla.edu

B. Hu, S. H. Tolbert, B. S. Dunn
Department of Materials Science and Engineering
University of California, Los Angeles
Los Angeles, CA 90095, USA
E-mail: bdunn@ucla.edu

G. la Diaz De la Cruz, B. C. Thompson, S. R. Narayan†
Department of Chemistry and Loker Hydrocarbon Research Institute
University of Southern California
Los Angeles, CA 90089-1661, USA

The ORCID identification number(s) for the author(s) of this article can be found under https://doi.org/10.1002/admi.202500098

†deceased May 24, 2023.

DOI: 10.1002/admi.202500098

of molecules.[21,22] For *p*-type conjugated polymers, scanning to potentials higher than the open circuit voltage will oxidize the polymer, generating regions of +1 charge carriers throughout the polymer. When an electron is removed from the π-system of a semiconducting polymer, the polymer backbone locally changes to accommodate the added charge, converting from an aromatic to a quinoid structure.[23,24] This leads to the formation of two localized energy levels within the bandgap. The charge carriers that are produced upon doping and the lattice distortion together are known as a polaron.[25] When the polymer is further oxidized, bipolarons, or doubly-charged spinless charge carriers, can form.[26] The existence of bipolarons is easily observed in the CV curve as a second oxidation peak at a higher potential.[27] Bipolarons are typically more difficult to form via chemical doping than polarons due to anion ordering, but electrochemically, they form easily by simply increasing the applied potential.[14,27–29] Past studies have shown that while bipolaron formation can significantly alter the structure of semiconducting polymers, these charge carriers are typically less electrically conductive than polarons.[15,30]

As discussed above, when doping semiconducting polymers, whether electrochemically or chemically, a counterion must enter the polymer matrix for charge neutrality.[31,32] In conventional *p*-type chemical doping, a dopant molecule, D, oxidizes the polymer backbone, and the reduced dopant molecule, D^-, stays in the polymer matrix to counterbalance the *p*-polaron. In electrochemical doping, the semiconducting polymer is submerged in an electrolyte containing a salt that is generally well dissociated. For example, lithium bis(trifluoromethanesulfonimide) (LiTFSI) is a common electrolytic salt that readily forms separated Li^+ and $TFSI^-$ ions in non-aqueous electrolyte solutions. When the semiconducting polymer is oxidized, $TFSI^-$ can be pulled into the polymer matrix to balance the positive charge.[33,34] For this to occur, ion mobility in the polymer matrix is needed. In previous studies,[35,36] we found that semiconducting polymers that readily swell more in the electrolyte also have higher ionic conductivity.

Many electronic applications of semiconducting polymers require reversible electrochemical doping of the polymer. Conjugated polymer-based sensors are one such application, with potentiometric[37] and colorimetric[38] sensors as two such examples. In potentiometric sensors, the sensitivity of doped polymers to electrostatic interactions allows for the detection of changes to analyte concentrations by tracking the chemical potential of the conjugated polymer. Colorimetric sensors can either be chemically or electrochemically doped,[39] and take advantage of the fact that the neutral and oxidized polymer states are visually distinctly different. Organic electrochemical transistors (OECTs) also require reversible electrochemistry with a semiconducting polymer.[40] Here, the semiconducting polymers form the channel, and electrochemical doping is used as the gate.[41]

Batteries are another electrochemical application that require reversible polymer doping. Semiconducting polymers can act as the active material, electrolyte, or binder in a battery.[6,42] One function in which they show the most promise is their utilization as binders. Currently, the most commonly used battery binder is polyvinylidene fluoride (PVDF).[43] While PVDF provides mechanical support while being chemically stable at a large potential range, it does not offer much benefit in terms of electron or ion mobility.[44] By utilizing semiconducting polymers, the polymer binder can still satisfy the need for mechanical support and chemically inertness, while increasing electronic and sometimes ionic conductivity.[17,35,45] For all battery applications, the electrolyte is always in contact with the semiconducting polymer, which means that the performance of these materials is intimately connected with the way they swell.

The need to further understand and control conjugated polymer swelling during electrochemical doping in device applications has been recognized in the literature. In most cases, researchers address this concern by designing polymers with the addition of sidechains,[46–48] functional groups,[49] or taking advantage of cross-linking,[50] to control solvent uptake. However, the degree of conjugated polymer swelling, especially in electrochemical systems, is not static. Electrolytes are polar and doped polymers with added charges are more polar than their undoped, neutral counterparts. As such, swelling is a dynamic phenomenon that changes during doping, gating, and/or cycling. For example, it was shown that an *n*-type polymer, poly(benzimidazobenzophenanthroline) (BBL) incorporates water molecules into the crystalline regions of the polymer film, creating a hydrophilic microenvironment within a hydrophobic polymer network, aiding in fast ion transport with aqueous electrochemical doping.[51] Other studied examined static swelling of poly(3,4-ethylenedioxythiophene) polystyrene sulfonate (PEDOT:PSS) in a variety of solvent environments, where they found that electrolytic solvents swell the polymer mixture more than pure solvent systems.[52] Swelling during electrochemical doping in this system was also examined, and showed that PEDOT:PSS films increased in thickness with applied potentials. Conjugated polymers swelling can also be controlled by changing the ratio of glycol and alkyl sidechains.[35,50] Because of the importance of swelling for ion mobility, it results in an optimization challenge: semiconducting polymer must swell enough easily as it becomes doped so that they show good electronic conductivity, but too much solvent uptake can result in a decrease in electronic conductivity. Excessive solvent uptake leads to polymer dissolution.[53]

A variety of parameters can affect polymer swelling, such as the initial crystallinity or regioregularity of the polymer, the side chain composition, and the choice and concentration of the electrolyte and the solvent.[48,50,54] The initial crystallinity also affects the electronic behavior of the polymer; typically, more crystalline or more regioregular polymers are more easily doped than their less crystalline counterparts.[55–57] Although higher crystallinity or regioregularity polymers may have lower oxidation potentials, they also swell less, providing a kinetic barrier to counterion intercalation. These factors all contribute to the ability of semiconducting polymers to conduct ions.

While there are many studies, specifically in the organic electrochemical transistor (OECT) literature that consider polymer swelling and its role in facilitating fast polymer doping, many simplify the challenge to a static problem that can be solved by engineering polymer side chains to control polymer swelling. Only a few groups take into consideration that swelling is dynamic and changes as the semiconducting polymer is doped and becomes charged.[58–60] However, these studies are usually performed in

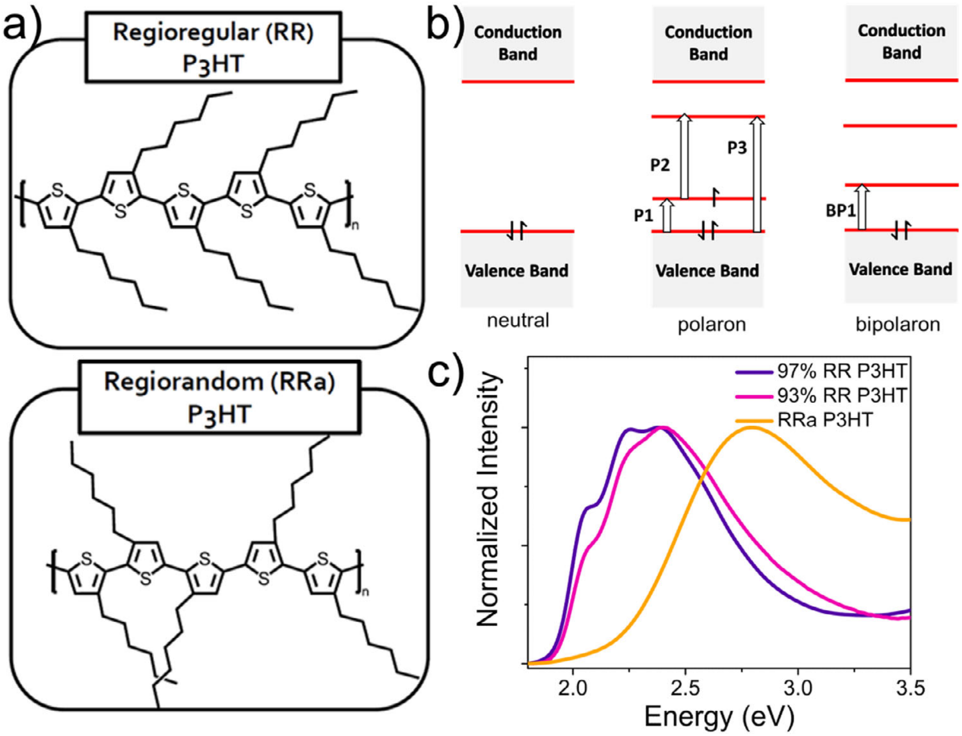

Figure 1. a) The chemical structure of regioregular (RR) and regiorandom (RRa) P3HT, b) the bandgap and inter-bandgap transitions for neutral, polaron doped, and bipolaron doped polymers, and c) UV/Visible absorption spectra of P3HT with different regioregularities showing different vibronic features.

aqueous media, and there is a significant lack of understanding of dynamic swelling in organic solvents. As a result, here, we study dynamic swelling during doping using an electrochemical quartz crystal microbalance (EQCM). The work uses a model conjugated polymer system, poly(3-hexylthiophene) (P3HT chemical structures shown in **Figure 1a**) in a range of organic electrolytes, including both standard battery electrolytes and more conventional organic solvents. We first examine the electrochemical behavior of P3HT with three different regioregularities, and show how these polymers are doped with increasing oxidizing potential. We then use spectro-electrochemistry to show how polaron and bipolaron formation can be controlled through the applied doping potential. Through grazing incidence wide-angle X-ray scattering (GIWAXS), we show how these polymers undergo structural changes with doping, observing both increases and decreases in their crystallinity. We use an in situ EQCM to directly visualize how the applied potential and thus, the doping level, dynamically affects the swelling of P3HT of differing regioregularities, and in different solvents. EQCM is a unique tool which measures mass change information near the resonator surface, and is the best option to study swelling in polymer thin films.[61–66] The results clearly demonstrate that swelling is a dynamic process influenced by electrochemical potential, rather than a static phenomenon and that bipolaron formation is strongly correlated with increased swelling. In situ measurement of electronic and ionic conductivities corroborate the impact of swelling on these macroscopic properties. Swelling enhances ionic conductivity, but is unfavorable for electronic conductivity. Collectively, this work highlights the strong correlation between doping, swelling, and conductivity.

2. Results and Discussion

The overarching goal of this work is to understand how solvent uptake changes during electrochemical doping in a range of solvent environments, and how that uptake controls polymer properties. Previous studies have shown that different solvents can swell polymers by varying amounts,[48,54] but this work aims to understanding that swelling as a dynamic process that changes during the electrochemical doping. To do this, we examine electrochemical doping of polymers with varying crystallinity, under a range of potential, using a variety of electrolytes with different solvents and different salt concentrations. To gain a deeper understanding of how solvent uptake affects polymer properties during electrochemical doping, we employ a range of characterization techniques. Among these, spectro-electrochemistry is particularly valuable for tracking doping-induced changes in the polymer's electronic structure in real time.

2.1. Spectro-Electrochemistry of P3HT

When semiconducting polymers are doped, either chemically or electrochemically, their optical signatures change, as shown in Figure 1b. When this occurs, singly charged polarons are formed on the polymer backbone, and three new absorption features appear: P1, P2, and P3, which result from interband transitions to or from the new polaron states in the gap. When the polymer is further doped, bipolarons can form, resulting in the appearance of yet another optical band (BP1), which appears slightly to the blue of P1. It is sometimes challenging to form bipolarons through chemical doping, but they form readily under

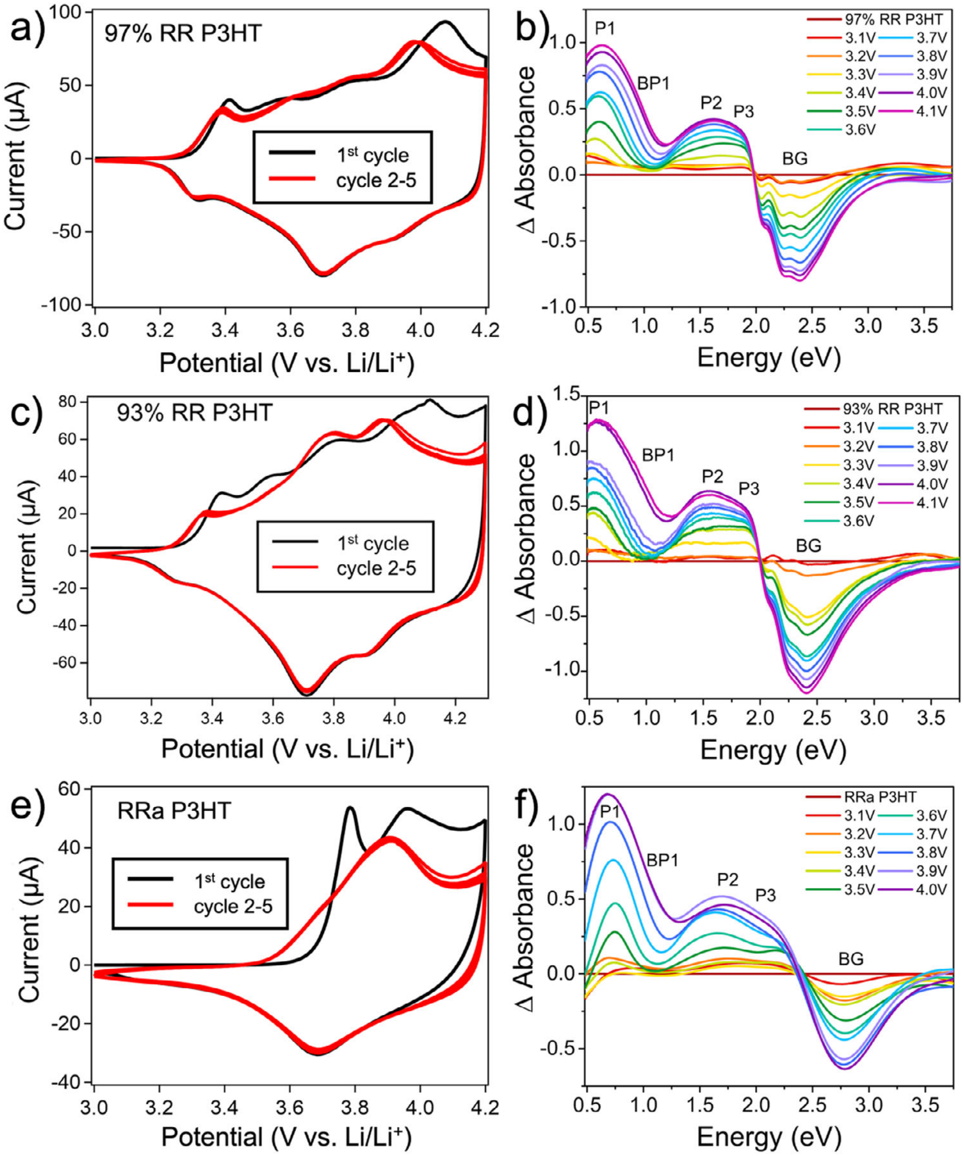

Figure 2. Electrochemical and spectro-electrochemical characterization of P3HT. Panels a, c, and e show the CV data, and panels b,d, and f showing differential UV-visible-near IR absorption as a function of applied potential. Panels a-b correspond to 97% RR, c,d) to 93% RR, and e,f) to RRa P3HT. UV-visible-near IR absorption data are shown as absorbance difference versus the undoped polymers in (b),(d), and (f). All absorption data was collected on cycle 6.

electrochemical conditions. Here, we consider three P3HT samples with different regioregularities: 97% regioregular (RR), 93% RR, and regiorandom (RRa). The most regioregular should also be the most ordered polymer, while inconsistent regiochemistry frustrates chain packing. The neutral polymer absorption spectra of each polymer are shown in Figure 1c, providing evidence that the most regioregular polymer is the most ordered, as indicated by the decrease in the vibronic features decreasing going from 97% RR to 93% RR to RRa.[67,68] Additionally, for RRa P3HT, the bandgap peak (or π–π* transition) shifts to higher energy due to the shorter conjugation length associated with increased defects in the polymer structure.

Figure 2a,c,e shows cyclic voltammograms (CV) of the three P3HT samples. Here, and everywhere else, unless specified otherwise, the electrolyte was 1 M LiTFSI in a mixture of ethylene carbonate (EC) and dimethyl carbonate (DMC) (see experimental section for details). For the two regioregular P3HTs, Figure 2a,c, the CV shows four oxidation peaks. To understand what charge carriers are being formed during these oxidative events, the optical signatures at each potential were examined using UV/Visible/Near IR absorption spectroscopy, as shown in Figure 2b,d,f for 97%, 93%, RRa, respectively. For the 97% RR material, the polymer becomes very slightly doped starting at 3.1 V versus Li/Li$^+$ and remains at a similar doping level until 3.4 V versus Li/Li$^+$, after which the P1, P2, and P3 peaks grow significantly. For all cycles after the first one, 3.4 V is the potential at which the first oxidative peak appears at in the CV. From there until ≈3.8 V versus Li/Li$^+$, these inter-bandgap peaks continue

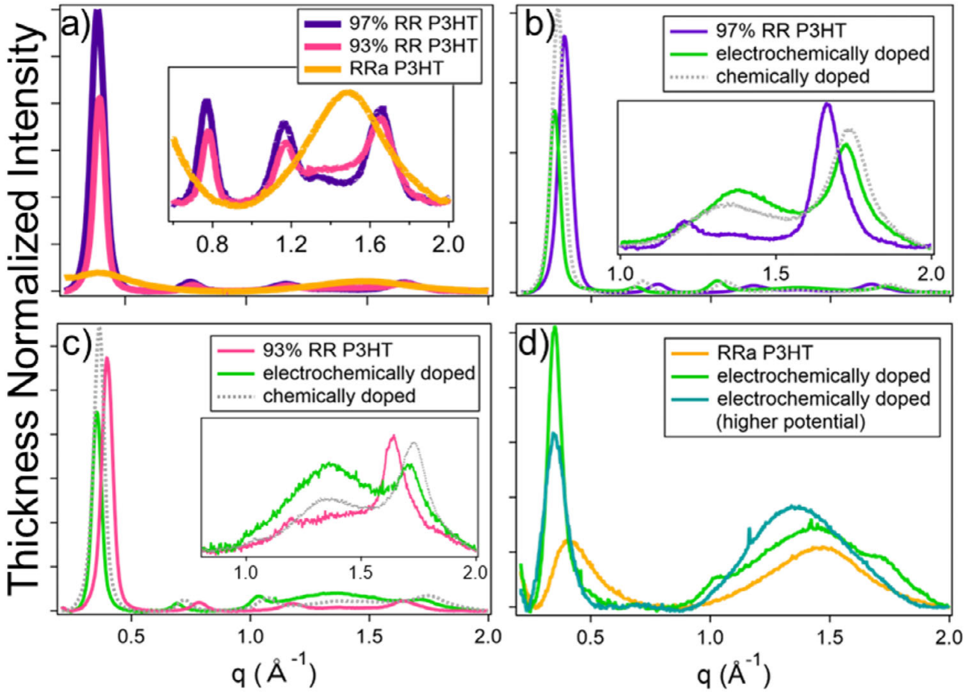

Figure 3. Thickness normalized GIWAXS data for a) the three neutral polymers before doping, b) 97% RR P3HT before doping (purple trace), electrochemically-doped (green trace), and chemically-doped (gray trace), c) 93% RR P3HT before doping (pink trace), electrochemically-doped (green trace), and chemically-doped (gray trace), and d) RRa P3HT before doping (yellow trace), electrochemically-doped at a low potential (green trace), and electrochemically-doped at a higher potential (teal trace).

to grow in, indicating that additional polarons are being formed. After 3.8 V, however, the P2 peak plateaus, and a blue shoulder appears on the side of the P1 band, which can be assigned to BP1. The normalized absorption in the P1 region can be found in Figure S1 (Supporting Information). The data first show a shift of the P1 peak to the blue at low doping potentials. This blue shift in P1 has been attributed to less delocalized carriers,[69] and is to be expected as more trapped polarons form in less ordered polymer regions at higher potentials. At even higher potentials, the P1 peak center stops shifting, and instead a blue shoulder appears. From the band diagram shown in Figure 1b, as well as previous studies, this blue shoulder has been attributed to the formation of bipolarons and is assigned to the BP1 peak.[14,27] Similar behavior is seen in the 93% RR P3HT (Figure 2d), but at slightly increased applied potentials. Thus, the first two redox peaks are associated with polaron formation, likely in the crystalline and amorphous regions of the polymer respectively,[70,71] and the higher redox peaks are associated with bipolaron formation. We note that the first cycle of each polymer (black traces) differs from the rest of the cycles. For the two regioregular polymers, the key difference between cycle 1 and later cycles is a shift in all redox peaks to lower potential. The RRa samples show more differences, which are discussed below. Because of these changes, all absorption, diffraction, and EQCM data was collected after precycling the samples.

The RRa P3HT sample shows quite different behavior to that seen with the regioregular material. The most dramatic difference is the loss of a redox peak and the large shift to lower potential between the first cycle and subsequent cycles in Figure 2e. Ignoring, for the moment, the first cycle data, the absorption difference spectra in Figure 1f shows that at 3.5 V versus Li/Li$^+$, the P1 and P2 bands both grow in, notably without the bluer intensity that is associated with P3 above. The blueshift in the P1 can be attributed to more localized polarons, which is expected with a more disordered polymer. Interestingly, at 3.5 and 3.6 V versus Li/Li$^+$, there is also a defined peak in the absorption spectra at ≈2.3 eV, which we associate with a red shifted bandgap absorption. Although the BP1 transition is not as obvious in the RRa sample because of the blue shifted P1 peak, there is a clear blue shoulder that forms at ≈3.9 V versus Li/Li$^+$, a potential that also corresponds to the oxidation peak in the CV. Thus, despite the fact that the CV curve for the RRa after cycle 1 is rather broad and featureless, the optical absorption still clearly indicates the formation of polarons at lower potentials and the formation of bipolarons at higher potentials, similar to the RR samples.

2.2. Structural Changes Upon Electrochemical Doping

Changing the regioregularity changes the crystallinity of the polymer,[72] as demonstrated in **Figure 3**a, shows the thickness normalized GIWAXS patterns of the different P3HT polymers studied in this work. This technique allows for direct visualization of the polymer structure and how it changes with electrochemical doping. Figure S2 (Supporting Information) shows the 2D diffraction patterns of the neutral and electrochemically doped polymers, where the two regioregular polymers are highly textured, with an edge-on crystallite orientation, while the RRa polymer is mostly amorphous and untextured. The thickness normalized GIWAXS patterns in Figure 3a confirm that both regioregular samples are quite crystalline, while the RRa P3HT is mostly amorphous. For the crystalline samples, a progression of lamellar peaks can be observed starting at $q \approx 0.4$ Å^{-1}, and a π-stacking peak is clearly seen at $q \approx 1.7$ Å^{-1}. In the RRa case, a low intensity lamellar peak with no overtones is observed near q -≈ 0.4 Å^{-1}, along with a broad peak around $q \approx 1.4$ Å^{-1}.[73]

Figure 3b,c show the 97% and 93% RR P3HT, respectively, doped electrochemically (green trace) and doped chemically using the standard oxidizing agent $FeCl_3$ (gray trace). Chemically doped samples are included as a reference for the standard structural changes expected upon polaron formation. With these two regioregular forms of P3HT, the electrochemically-doped samples show similar peak shifts to the chemically doped samples, indicating that the structure at the end of doping (whether chemical or electrochemical) is similar. These structural changes arise because the polymer must accommodate the insertion of a counteranion into the polymer crystallites to stabilize the positive charge formed on the polymer backbone.[68,74] In the electrochemical case, LiTFSI was used as the electrolytic salt, so TFSI$^-$ is the counterion in the polymer. For both the 93% and 97% RR P3HT, electrochemical doping results in a slightly more intensity in the broad disordered π-stacking peak, indicating that electrochemical doping disrupts the polymer crystallinity more than chemical doping. The appearance of more diffuse/amorphous scattering is accompanied by a reduction in the diffraction intensity of the crystalline diffraction peaks. This can be seen most easily by the reduction in the lamellar peak intensity at $q \approx 0.4$ Å^{-1}. The two regioregular polymers change similarly upon electrochemical doping. We note that this intensity decrease is not intrinsic to the doping process, as the chemically doped samples actually show an increase in lamellar peak intensity. As discussed below, the disordering likely stems from repeated solvent swelling by the electrolyte across the first few CV cycles.

In the RRa case (Figure 3d), the polymer starts off rather amorphous, but upon electrochemical doping (green trace), there is a significant increase in the crystallinity. The lamellar peak around $q \approx 0.4$ Å^{-1} grows dramatically in intensity, and in the π-stacking region, the formation of a distinct π-peak at $q \approx 1.75$ Å^{-1} shows that regular stacking is induced by electrochemical doping. At higher potentials, where bipolarons should be formed (blue trace), the overall intensity decrease slightly, as compared to the lower potential electrochemically-doped case (green trace), but most of the new diffraction intensity remains. This result is not surprising, as doping induced crystallization has been observed previously in RRa P3HT.[57,75–77] In chemically doped samples, that crystallization appears to be reversible upon thermal de-doping,[74] but based on the fact that the CV curve changes after the first cycle and then remains stable, we hypothesize that doping induced crystallization in electrochemically doped RRa P3HT is not reversible and thus all RRa data presented here, other than that explicitly collected during the first cycle, should be assumed to be on crystallized samples.

2.3. Tracking of Dynamic Swelling via EQCM

To understand how the structural changes seen with GIWAXS is connected to solvent swelling, we look at how the polymer mass change with electrochemical potential via EQCM. This experiment can measure the change in mass with applied potential, which can be used to calculate the *change* in solvent swelling upon doping; it is important to note that the solvent swelling prior to data collection in the undoped polymer is unknown. The total mass change detected by EQCM for the different P3HT samples as a function of applied bias (black curves in **Figure 4**) comes from a combination of the incorporated TFSI$^-$ anions, which are needed to counterbalance the polaronic charges, and any solvent molecules that swell the film. Here, we assume that these are the only two species participating in the mass change and that each positive charge created during doping attracts a single TFSI$^-$, as it has been assumed before for aqueous systems.[59,60] However, it is important to note that this extra mass assigned to pure solvent could have some component of the electrolyte neutral salt. While we will refer to it as "solvent mass" throughout this work, it may contain some LiTFSI, particularly in cases with very high solvent swelling. Based on this assumption, we can integrate the CV curves to determine the number of created charges, and then convert that into the mass of adsorbed TFSI$^-$ (see the Supporting Information for details). The mass change expected from the adsorbed TFSI$^-$ is shown by the light grey curves in Figure 4. As shown in all Figure 4 panels, black curves do not overlap the light grey curves, which indicates that the overall mass change cannot be ascribed only to the anion mass change. The difference between the black and grey curves must be due to mass change from doping-induced solvent swelling; these mass changes are shown as the blue curves.

During the polaron formation region between 2.85 and 3.20 V for RR P3HTs and 2.85 and 3.35 V for RRa P3HT, shown in Figure 4a–c, the EQCM data shows a small or zero mass increase, followed by a mass decrease for all three P3HT regioregularities. The 97% and 93% RR P3HT show the most similar data, with a small mass increase that correlates with the first polaron formation peak, and then a decreases at the second polaron formation peak. This data is in good agreement with the idea that the first redox peaks correspond to polaron formation in the crystalline regions of the polymer, and the second to the formation of polarons in the amorphous region. Polaron formation should increase polarity and thus increase solvent swelling in polymer crystallites. The amorphous regions should already be highly swollen, as amorphous polymers are much easier to swell/dissolve than their crystalline counterparts. As shown in Figure 3d, when amorphous polymers become doped, they become more crystalline, and so if the second redox peak corresponds to doping of the amorphous regions, it should be accompanied by increased crystallization, which should force some solvent to be expelled from the polymer network. Thus, while the mass appears to increase and decrease, this is not a reversible process, but instead one that corresponds to increased solvent swelling in the crystalline regions and decreased solvent swelling in the formerly-amorphous regions.

For RRa P3HT, the mass shows almost no increase in the first region where redox occurs, followed by a more significant

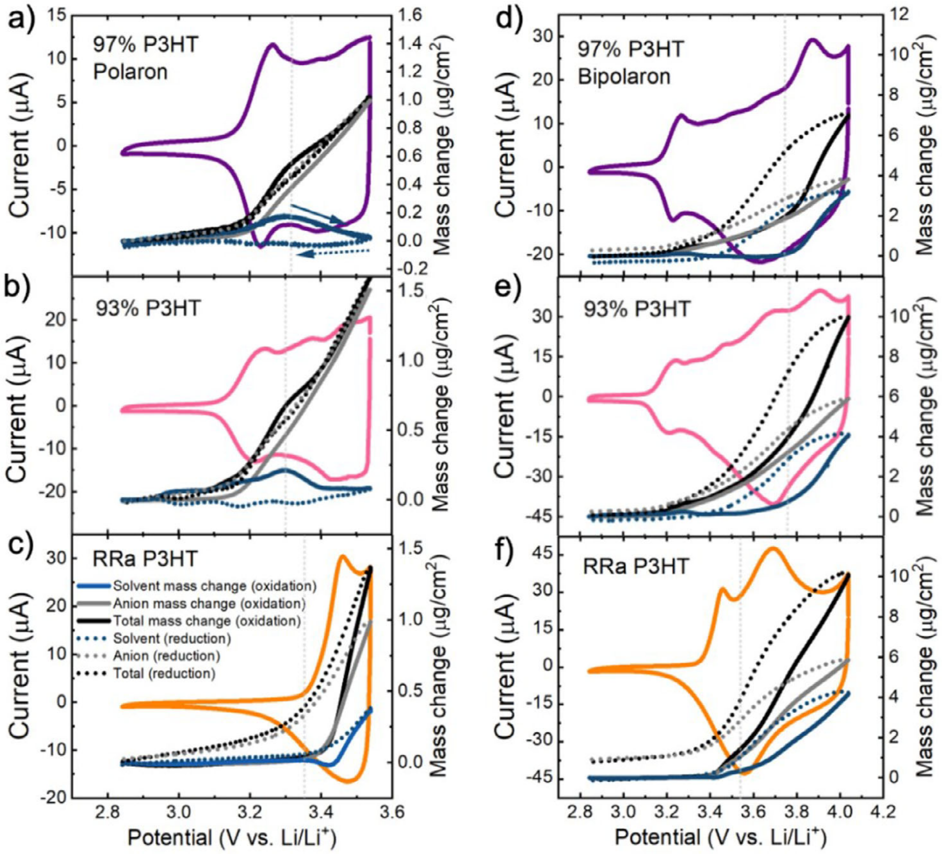

Figure 4. CV (colored) and EQCM data for a,d) 97% RR, b,e) 93% RR, and c,f) RRa P3HT at a–c) polaron-forming potentials and d–f) the full range of potentials, including those where bipolarons are formed. The black curves indicate the total mass change, as reported by EQCM. The light gray curves are derived from integration of the CV curve using the assumption that every 1 e^- requires 1 TFSI$^-$ molecule to be pulled into the polymer network. The blue curves correspond to mass of solvent entering the polymer matrix, and are calculated as the difference between the black and grey curves. Solid lines indicate data collected during forward bias in the oxidative direction, while the dotted lines correspond to data collected in the reverse, reductive direction.

negative mass change at higher potentials. We can understand the very small initial mass increase by the fact that the RRa material should be more disordered than the RR polymers, even after doping-induced crystallization, and so they are likely fully solvent-swollen at the start of the cycle with little additional solvent uptake observed. The mass loss at higher potentials is assigned to reversible doping-induced crystallization, similar to the amorphous polaron peak in the regioregular polymers.

To understand the connection between polaron formation and swelling more quantitatively, we calculate the ratio of the solvent mass change to the TFSI$^-$ mass change. For crystalline polaron formation, this ratio is 0.52, 0.46, and 0 ug/ug for 97%, 93% RR P3HT, and RRa P3HT, respectively; for amorphous polaron formation, it is -0.23, -0.31, -0.24 μg/μg for 97%, 93% RR P3HT, and RRa P3HT, respectively. This shows that 97%, 93% RR P3HT experience similar solvent swelling during polaron formation in crystalline, and that doping induced crystallization results in similar solvent expulsion in all 3 samples during doping of the amorphous regions. The only unique behavior is the solvent neutral doping of the partly crystallized RRa material.

In Figure 4a–c, the polymers were only cycled in the polaronic electrochemical window to understand how polaron formation changes the swelling behavior of conjugated polymers. To understand the swelling when bipolarons are formed, the polymers were cycled across the entire electrochemical window where the polymer remains stable. Figure 4d–f indicates that for all three P3HT samples, bipolaron formation is accompanied by much more dramatic solvent swelling than polaron formation. We have shown previously using theoretical methods, that bipolarons only form when two counterions can get physically close to one another, a process that often requires disordering of the polymer crystallites.[27] In order to induce such significant disorder in the polymer network upon chemical doping, significant solvent swelling is likely required to reduce both the kinetic barriers to and thermodynamic cost of breaking up the polymer crystallites. Here, upon electrochemical doping, it appears that such disordering may also be occurring, and that the disordering is again intrinsically tied to solvent swelling. The bipolaron solvent-swelling-to-TFSI$^-$ mass ratio is 0.83, 0.71, and 0.72 μg/μg for 97% RR P3HT, 93% RR P3HT, and RRa P3HT, respectively. These values are all much higher than those observed during polaron formation. It is also interesting to note that the total solvent swelling is greater for the 93% RR and RRa P3HT at 4.0 V versus Li/Li$^+$ than for the 97% RR P3HT, and that after bipolaron

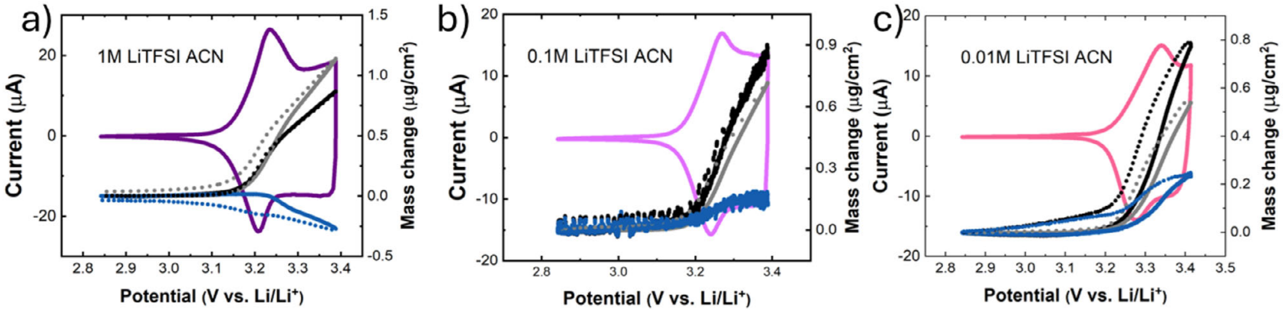

Figure 5. CV (colored) and EQCM data of 93% RR P3HT at polaron-forming potentials, cycled in a) 0.01 M LiTFSI, b) 0.1 M LiTFSI, and c) 1 M LiTFSI in acetonitrile. The black curves indicate the total mass change, as reported by EQCM. The light gray curves are derived from integration of the CV curve using the assumption that every 1 e^- requires 1 $TFSI^-$ molecule to be pulling into the polymer network. The blue curves correspond to mass of solvent entering the polymer matrix, and are calculated as the difference between the black and gray curves. Solid lines indicate data collected during forward bias in the oxidative direction, while the dotted lines correspond to data collected in the reverse, reductive direction.

formation, the 93% RR and RRa P3HT films show the same solvent swelling.

In addition to polymer crystallinity and doping level, ionic strength and the nature of the solvent could be other major factors affecting solvent swelling. Thus, here we investigated the role of the solvent and of the concentration of LiTFSI, this time using acetonitrile (ACN) to make the electrolyte solution. We have previously reported that ACN does not swell neutral 93% RR P3HT to a measurable extent.[27] However, when doped, ACN can swell 93% P3HT to a larger extent. Indeed, ACN swells P3HT to such a large extent during bipolaron formation that the film becomes jelly-like, and the energy dissipation becomes too large to accurately measure the mass.[78,79] However, by limiting the potential window at crystalline polaron formation, the swelling of P3HT by ACN in various concentrations of LiTFSI can be identified. For these experiments, the same methods were used as for Figure 4, where the mass change was measured by EQCM, the $TFSI^-$ mass was calculated from the CV curve, and the difference was assigned to solvent swelling.

In comparing Figure 4b to **Figure 5a**, both of which were collected on 93% RR P3HT cycled in a 1 M LiTFSI electrolyte, the most obvious difference is that the data collected in EC:DMC shows solvent swelling during polaron doping of the crystalline regions, followed by deswelling during the dopant induced crystallization of the amorphous regions. In contrast, the initial solvent swelling region does not appear when ACN is used, and only the solvent deswelling is observed. The result is reasonable, because we have established previously that ACN is a poor swelling solvent for crystalline P3HT. Interestingly, as the ionic strength is lowered, the solvent deswelling between 3.25 and 3.4 eV versus Li/Li^+ is gradually replaced by a small amount of solvent swelling. We can understand these changes in swelling by considering the relative free energy of the electrolyte in solution, versus in the film. At higher salt concentration, the ACN is entropically (osmotically) stabilized in the electrolyte phase; this should make it more favorable for the ACN to reside in solution compared to in the polymer film, and should favor deswelling of the polymer films at high salt concentrations. Moreover, in highly concentrated LiTFSI solutions, solvent molecules are also more tightly coordinated to lithium ions, leading to increased enthalpic stability within the solvation shell, which should again favor solvent deswelling at higher salt concentrations.[80] Both of these effects should make it easier to pull ACN out of the polymer film upon doping induced crystallization. As the LiTFSI concentration decreases, this driving force for solvent expulsion also decreases, allowing a small amount of solvent swelling to be observed in the more dilute electrolytes with increasing doping levels and thus increasing polymer polarity. The result thus emphasizes the delicate balances that control dynamic solvent swelling during electrochemical doping of conjugated polymers.

2.4. Electrical and Ionic Conductivity Measurements

Conjugated polymer swelling is an important factor to consider for both electronic and ionic conductivity. Swelling aids in the intercalation of anions into the polymer matrix, thus should increase ionic conductivity.[35] On the other hand, swelling of crystalline regions can disrupt π-stacks, which are key electronic pathways. As a result, too much solvent uptake could result in lower electronic conductivity.[35] To better understand these effects, ionic and electronic conductivities were measured on the three P3HT regioregularities as a function of electrochemical doping potential, as shown in **Figure 6**. Data was collected using polymer films deposited on interdigitated gold electrodes that could either be shorted together for electrochemical doping, or separated to measure electronic and ionic conductivity via impedance spectroscopy, all while immersed in electrolyte. More details on the method are presented in the SI and have been published previously.[81] Data was collected in 0.1 V increments between 3.0 to 4.0 V versus Li/Li^+. Representative Nyquist impedance plots are shown in Figure S3, fitting parameters are given in Tables S1,S2, and the electronic and ionic conductivity values are listed in Tables S3–S8 (Supporting Information).

In the fully doped state, the most regioregular polymer, 97% RR P3HT, shows the highest electrical conductivity value of 0.263 S cm^{-1} (Figure 6a). This value is more than an order of magnitude lower than values obtained on similarly doped samples measured under dry conditions, indicating that solvent swelling significantly reduces electrical conductivity.[82] The peak electronic conductivity of 93% RR P3HT and RRa P3HT are essentially the same (Figure 6a), likely because when fully doped,

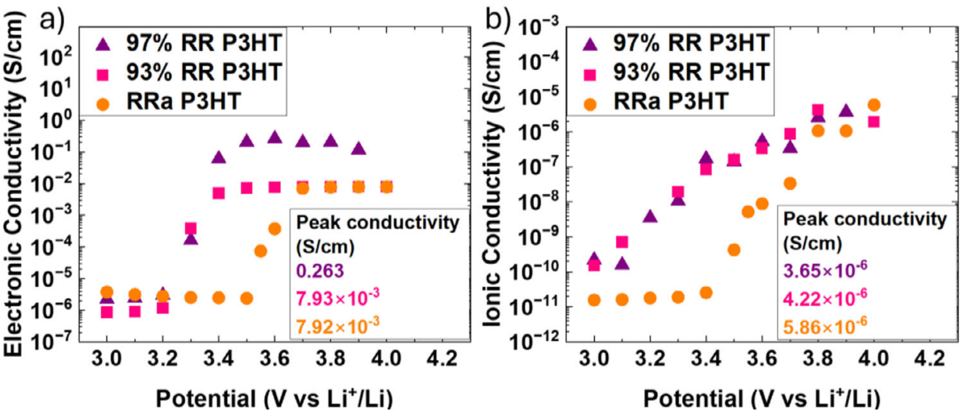

Figure 6. a) Ionic and b) electronic conductivity of 97% (purple), 93% (pink), and RRa (orange) collected at 0.1 V increments in the 3.0 to 4.0 V versus Li/Li$^+$ potential range. RRa P3HT has the highest ionic conductivity while 97% RR has the highest electronic conductivity.

they both show the same total solvent swelling, and solvent swelling dominates the electrical conductivity under these conditions. In agreement with the CV curves shown in Figure 2, the electrical conductivities of all samples show a sharp rise where the polymers start to dope. This corresponds to a potential of ≈3.3 V versus Li/Li$^+$ for the RR materials, and a potential of ≈3.5 V versus Li/Li$^+$ for the RRa material. Interestingly, at very low potentials, the RRa sample shows the highest electrical conductivity (Figure 6a). This is likely because the very disordered RRa material is quite difficult to fully dedope; the disordered regiorandom polymer network contains many deep-trap sites that would require much lower reducing potentials to fully remove all polarons.[83,84] As a result, some low residual doping level remains after a full CV cycle, leading to a small but measurable conductivity before the main doping redox peak.

The ionic conductivities can also be well understood by considering solvent swelling. For 97% and 93% RR P3HT, ionic conductivity increases steadily with increasing potential, peaking at values of 3.65×10^{-6} and 4.22×10^{-6} S cm^{-1}, respectively (Figure 6b). The slightly lower value for the 97% RR P3HT correlates with the lower solvent swelling and the higher electronic conductivity in this material. The slow increase starts at 3.1 V versus Li/Li$^+$ for the 97% RR P3HT, and at 3.0 V versus Li/Li$^+$ for the 93% RR P3HT, in excellent agreement with the EQCM data, which shows that solvent swelling begins at 2.9 V versus Li/Li$^+$ for 93% RR P3HT and at 3.0 V versus Li/Li$^+$ for 97% RR P3HT. Clearly, solvent swelling is the key to facilitating ionic conductivity. For the RRa P3HT, ionic conductivity is lower than for the RR P3HT samples (Figure 6b) and does not increase until 3.5 V versus Li/Li$^+$, where the oxidative peak starts (Figure 2e); it then increases steeply for the rest of the potential range, reaching a maximum of 5.86×10^{-6} S cm^{-1}. This is the highest ionic conductivity of any of the samples, in agreement with the more disordered nature of the RRa sample. The fact that the ionic conductivity starts low and does not begin to increase until 3.5 V versus Li/Li$^+$ is again in good agreement with the EQCM data, which shows that solvent swelling does not begin in RRa P3HT until 3.5 V versus Li/Li$^+$. Overall, the ionic conductivity data indicates that doping induced solvent swelling is required for good ionic conductivity in these materials.

3. Conclusion

Although swelling of polymers is well recognized in the literature as an important factor impacting macroscopic properties such as ionic conductivity,[35,59] swelling is usually controlled by altering materials properties, such as by tuning the polymer sidechains or introducing cross-linking. However, this work shows clearly that swelling is a dynamic process that changes not only with polymer crystallinity, but also with electrolyte concentration, solvent choice, and doping level. To explore this dynamic process, we examined electrochemical doping in P3HT samples of three different regioregularities, which translated to three different initial degrees of crystallinity. Despite differences in the exact redox potentials, all samples could be electrochemically doped to form polarons at lower potentials, and to form bipolarons at more oxidizing potentials. EQCM results were then used to examine solvent swelling as a function of doping level. At the lowest doping levels, the most crystalline samples pulled in solvent as they were doped because of the increased polarity, while more disordered samples showed no change in solvent swelling. At higher potentials, doping induced crystallization of formerly amorphous regions resulted in solvent expulsion in all materials. Lowering the electrolyte ionic strength, however, reduced the osmotic driving force for this solvent expulsion. Finally, once potentials high enough to induce bipolaron formation were reached, all samples pulled in significant amounts of solvent, in good agreement with the idea that the counterion locations needed to stabilize bipolarons generally result in disordering of the polymer crystallites, a process which should allow for additional solvent swelling.[27]

The impact of this swelling was then assessed using electronic and ionic conductivity measurements performed on polymers in electrolyte solutions. As expected, solvent swelling was found to be detrimental to electronic conductivity. Peak conductivity values were at least an order of magnitude lower than those obtained on dry films, despite similar doping levels. Moreover, films with lower solvent uptake showed higher electronic conductivity. The opposite was true for ionic conductivity, which showed a strong positive correlation with solvent swelling. The correlation was so strong, that it leads to the conclusion that doping induced solvent swelling is the primary factor controlling ion conductivity for these hydrophobic polymers in organic electrolytes. Overall, the results clearly show that solvent swelling can be dynamically controlled by the extent of doping and the nature of the polymer and electrolyte, and that significant optimization of ionic and electronic conductivity should be possible in solvent swollen semiconducting polymer films using these simple parameters.

4. Experimental Section

Materials: RRa and 93% RR P3HT was used as purchased from Reike, Inc.: RRa P3HT (4007), 93% (4002-EE). 97% RR P3HT was used as purchased from Ossila (M1011-1 g). Lithium bis(trifluoromethanesulfonyl)imide (LiTFSI), 99% was purchased from Fischer Scientific (originally part of Acros Organics portfolio); ethylene carbonate (EC) and dimethyl carbonate (DMC) were purchased from Sigma-Aldrich to be used in electrolyte preparation. $FeCl_3$ was purchased from EM Science to prepare chemically doped films. All polymer films were made from 20 mg mL^{-1} solutions in 1,2-dichlorobenzene (ODCB), spun at 1000 rpm for 55 s, 1500 rpm for 5 s. Films for electrochemical characterization and optical spectroscopy were spun on indium tin oxide (ITO, Delta Technologies, Limited, R_s = 10–15 Ω. Films for for grazing incidence wide-angle X-ray scattering (GIWAXS) were spun on Al-back-coated <100> oriented Si. Finally, films for electrochemical quartz crystal microbalance (EQCM) measurements were spun directly onto the gold electrodes of the EQCM resonators, purchased from BioLogic (AW-R10AU11P).

Characterization: All electrochemical experiments were performed using BioLogic potentiostats, in an Ar glovebox with O_2 and H_2O levels lower than 1 ppm. Cyclic voltammetry, electrochemical doping, and conductivity measurements were conducted on BioLogic VMP3. EQCM experiments utilized BioLogicSP-200.

Characterization—Cycling Voltammetry: Unless otherwise stated, BioLogic VMP3 was used to collect cyclic voltammograms, with the working electrode being the conjugated polymer on the necessary substrate, and the counter and reference electrodes being lithium metal. Unless otherwise stated, the potential range used was OCV (≈2.8 to 3.0 V) to 4.2 V versus Li/Li^+, with a scan rate of 10 mV s^{-1}. 1 M LiTFSI in EC:DMC (50:50 by v:v) is used as the electrolyte solution except for the ionic strength studies in Figure 4.

Characterization—UV-Visible Spectroscopy: For the 93 and 97% RR P3HT, a Shimadzu UV3101PC Scanning Spectrophotometer was used to acquire the *ex situ* UV/Visible/Near IR spectra. For RRa P3HT, the UV/Visible/Near IR spectra were collected on a Jasco V-770. The polymers were cycled 5 times and then held at the specified potential to dope in 1 M LiTFSI in EC:DMC. The films were then packaged in individual, seal vials to prevent dedoping upon transport to the spectrometer.

Characterization—Chemical Doping of P3HT Films: Chemically doped P3HT films were fabricated using sequential processing (SqP).[13] Undoped polymer films were prepared from either 97% or 93% RR P3HT solution in ODCB (20 mg mL^{-1}) by spin coating at 1000 rpm for 60 s. The films were then doped with 50 µL of a 1 mM $FeCl_3$ solution in n-butyl acetate by spreading the dopant solution on the film and allowing it to soak for 120 s, followed by spin-coating at 4000 rpm for 10 s to remove the excess dopant solution.

Characterization—Grazing Incidence Wide-Angle X-Ray Scattering (GIWAXS): GIWAXS measurements were performed at the Stanford Synchrotron Radiation Lightsource (SSRL) at beamline 11-3 using a wavelength of 0.9742 Å, 250 mm detector distance, and a He chamber to increase signal-to-noise. For all polymer films, an incidence angle of 0.12° was used. An Igor macro, Nika, was utilized to calibrate the GIWAXS data. Another Igor macro, WaxsTools was used to reduce the data. Each integration pattern is baseline subtracted, and all analysis was performed on Igor Pro.

Characterization—Electrochemical Quartz Crystal Microbalance (EQCM): BlueQCM QSD from BioLogic was used to detect mass change by monitoring the resonant frequencies of an oscillating quartz crystal. SP-200 potentiostat was used for cyclic voltammetry measurements during EQCM data collection. The reference electrode was Ag/AgCl, and the counter electrode was a platinum wire. The experiment was done in an inert Ar environment. The electrochemical quartz crystal microbalance (EQCM) was exploited to directly race the mass change with electrochemistry. The utilization of in situ EQCM-D (dissipation factor) techniques had been proven as a proficient means to enable real-time monitoring of ionic fluxes as well as solvent swelling during their polarization. As extensively elucidated, the accurate determination of mass changes through EQCM could only be achieved when gravimetric conditions were diligently upheld (ref). In this case, there should be zero or negligible dissipation changes. The negligible dissipation changes during the polarization indicates all the frequency changes collected were able to be converted into mass changes. The change in the measured frequency Δf has a linear dependence on the varied mass Δm, according to the Sauerbrey equation (Equation (1)):

$$\Delta f = -C_f \Delta m \tag{1}$$

where C_f is the sensitivity factor of the crystal, and Δm is the mass change per unit geometry area of the quartz crystal.

Characterization—In Situ Conductivity Measurements: The electronic and ionic conductivity were measured as a function of applied potential as previously reported. For both conductivity measurements, the polymer films were deposited on an interdigitated microelectrode from Metrohm DropSens (DRP-G-IDEAU5). The films were first electrochemically doped by applying the target potential for 300 s. For the measurement of electronic conductivity, the films were allowed to reach a steady open circuit potential after electrochemical doping, followed by an electrochemical impedance spectroscopy (EIS) measurement collected between 100 kHz and 100 mHz with an excitation of 10 mV at the two terminals of the interdigitated microelectrodes. For the measurement of ionic conductivity, EIS data with the same parameters was collected in the three-electrode cell immediately after electrochemical doping.

Supporting Information

Supporting Information is available from the Wiley Online Library or from the author.

Acknowledgements

C.Z.S. and B.H. contributed equally to this work. This work was supported by the Center for Synthetic Control Across Length-Scales for Advancing Rechargeables (SCALAR), an Energy Frontier Research Center funded by the U. S. Department of Energy, Office of Science, Basic Energy Sciences under Award #DE-SC0019381 (EQCM, impedance, and spectroelectrochemistry) and by the National Science Foundation under Awards DMR-2105896 and DMR-2513790 (GIWAXS). Use of the Stanford Synchrotron Radiation Lightsource, SLAC National Accelerator Laboratory, is supported by the U.S. Department of Energy, Office of Science, Office of Basic Energy Sciences under Contract No. DE-AC02-76SF00515. The authors thank SSRL for the use of Beamline 11-3.

Conflict of Interest

The authors declare no conflict of interest.

Data Availability Statement

The data that support the findings of this study are available in the supplementary material of this article and from the corresponding author upon reasonable request

Keywords

conjugated polymers, EQCM, GIWAXS, optical spectroscopy, P3HT

Received: January 31, 2025
Revised: March 30, 2025

---

[1] C. Yuan, Y. Zhou, Y. Zhu, J. Liang, S. Wang, S. Peng, Y. Li, S. Cheng, M. Yang, J. Hu, B. Zhang, R. Zeng, J. He, Q. Li, *Nat. Commun.* **2020**, *11*, 3919

[2] P. Rohland, E. Schröter, O. Nolte, G. R. Newkome, M. D. Hager, U. S. Schubert, *Prog. Polym. Sci.* **2022**, *125*, 101474.

[3] J. Kim, J. Lee, J. You, M.-S. Park, M. S. Hossain, Y. Yamauchi, J. H. Kim, *Mater. Horiz.* **2016**, *3*, 517c.

[4] A. M. Bryan, L. M. Santino, Y. Lu, S. Acharya, J. M. D'Arcy, *Chem. Mater.* **2016**, *28*, 5989.

[5] H. Sun, X. Guo, A. Facchetti, *Chem* **2020**, *6*, 1310.

[6] P. Das, B. C. Thompson, *Polym. J.* **2023**, *55*, 317..

[7] W. Kong, J. Wang, Y. Hu, N. Cui, C. Yan, X. Cai, P. Cheng, *Angew. Chem., Int. Ed.* **2023**, *62*, 202307622.

[8] W.-N. Wu, Q.-B. Zheng, C.-L. Liu, *Synth. Met.* **2024**, *307*, 117682.

[9] S. Griggs, A. Marks, H. Bristow, I. McCulloch, *J. Mater. Chem. C* **2021**, *9*, 8099.

[10] S. Brixi, O. A. Melville, B. Mirka, Y. He, A. D. Hendsbee, H. Meng, Y. Li, B. H. Lessard, *Sci. Rep.* **2020**, *10*, 4014.

[11] D. T. Duong, C. Wang, E. Antono, M. F. Toney, A. Salleo, *Org. Electron.* **2013**, *14*, 1330.

[12] K.-H. Yim, G. L. Whiting, C. E. Murphy, J. J. M. Halls, J. H. Burroughes, R. H. Friend, J.-S. Kim, *Adv. Mater.* **2008**, *20*, 3319.

[13] D. T. Scholes, S. A. Hawks, P. Y. Yee, H. Wu, J. R. Lindemuth, S. H. Tolbert, B. J. Schwartz, *J. Phys. Chem. Lett.* **2015**, *6*, 4786.

[14] C. Enengl, S. Enengl, S. Pluczyk, M. Havlicek, M. Lapkowski, H. Neugebauer, E. Ehrenfreund, *ChemPhysChem* **2016**, *15*, 3826.

[15] D. Tsokkou, P. Cavassin, G. Rebetez, N. Banerji, *Mater. Horiz.* **2021**, *9*, 482.

[16] B. D. Paulsen, C. D. Frisbie, *J. Phys. Chem. C* **2012**, *116*, 3132.

[17] P. Das, B. Zayat, Q. Wei, C. Z. Salamat, I.-B. Magdău, R. Elizalde-Segovia, D. Rawlings, D. Lee, G. Pace, A. Irshad, L. Ye, A. Schmitt, R. A. Segalman, T. F. Miller, S. H. Tolbert, B. S. Dunn, S. R. Narayan, B. C. Thompson, *Chem. Mater.* **2020**, *32*, 9176.

[18] O. L. Gribkova, V. A. Kabanova, O. D. Iakobson, A. A. Nekrasov, *Electrochim. Acta* **2021**, *382*, 138307.

[19] D. T. Christiansen, S. Ohtani, Y. Chujo, A. L. Tomlinson, J. R. Reynolds, *Chem. Mater.* **2019**, *31*, 6841.

[20] J. Gasiorowski, A. I. Mardare, N. S. Sariciftci, A. W. Hassel, *J. Electroanal. Chem.* **2013**, *691*, 77.

[21] N. Elgrishi, K. J. Rountree, B. D. McCarthy, E. S. Rountree, T. T. Eisenhart, J. L. Dempsey, *J. Chem. Educ.* **2018**, *92*, 197.

[22] B. Neelamraju, M. Rudolph, E. L. Ratcliff, *J. Phys. Chem. C* **2018**, *122*, 21210.

[23] A. Pron, G. Louarn, M. Lapkowski, M. Zagorska, J. Glowczyk-Zubek, S. Lefrant, *Macromolecules* **1995**, *28*, 4644.

[24] E. H. Suh, J. G. Oh, J. Jung, S. H. Noh, T. S. Lee, J. Jang, *Adv. Energy Mater.* **2020**, *10*, 2002521.

[25] C. Saporiti, L. Brambilla, D. Fazzi, C. Castiglioni, *J. Phys. Chem. C* **2024**, *128*, 5189.

[26] N. Colaneri, M. Nowak, D. Spiegel, S. Hotta, A. J. Heeger, *Phys. Rev. B* **1987**, *36*, 7964.

[27] E. C. Wu, C. Z. Salamat, O. L. Ruiz, T. Qu, A. Kim, S. H. Tolbert, B. J. Schwartz, *Adv. Funct. Mater.* **2023**, *33*, 2213652.

[28] J. L. Brédas, G. B. Street, *Acc. Chem. Res.* **1985**, *18*, 309.

[29] M. G. Voss, J. R. Challa, D. T. Scholes, P. Y. Yee, E. C. Wu, X. Liu, S. J. Park, O. L. Ruiz, S. Subramaniyan, M. Chen, S. A. Jenekhe, X. Wang, S. H. Tolbert, B. J. Schwartz, *Adv. Mater.* **2020**, *33*, 2000228.

[30] J. Yamamoto, Y. Furukawa, *Org. Electron.* **2016**, *28*, 82.

[31] T. Kawai, M. Nakazono, K. Yoshino, *J. Mater. Chem.* **1992**, *2*, 903.

[32] J. L. Thelen, S. L. Wu, A. E. Javier, V. Srinivasan, N. P. Balsara, S. N. Patel, *ACS Macro Lett.* **2015**, *4*, 1386.

[33] L. S. Hornberger, D. Neusser, C. Malacrida, L. G. Kaake, S. Ludwigs, *Appl. Phys. Lett.* **2021**, *119*, 163301.

[34] G. Pace, O. Nordness, K. Asham, R. J. Clément, R. A. Segalman, *Chem. Mater.* **2022**, *34*, 4672.

[35] P. Das, R. Elizalde-Segovia, B. Zayat, C. Z. Salamat, G. Pace, K. Zhai, R. C. Vincent, B. S. Dunn, R. A. Segalman, S. H. Tolbert, S. R. Narayan, B. C. Thompson, *Chem. Mater.* **2022**, *34*, 2672.

[36] P. Das, C. Z. Salamat, B. Zayat, R. Elizalde-Segovia, Y. Wang, X. Gu, S. R. Narayan, S. H. Tolbert, B. C. Thompson, *Chem. Mater.* **2024**, *36*, 1413.

[37] Á. Terán-Alcocer, F. Bravo-Plascencia, C. Cevallos-Morillo, A. Palma-Cando, *Nanomaterials* **2021**, *11*, 252.

[38] R. Sakai, *Polym. J.* **2016**, *48*, 59.

[39] D. T. McQuade, A. E. Pullen, T. M. Swager, *Chem. Rev.* **2000**, *100*, 2537.

[40] M. Moser, T. C. Hidalgo, J. Surgailis, J. Gladisch, S. Ghosh, R. Sheelamanthula, Q. Thiburce, A. Giovannitti, A. Salleo, N. Gasparini, A. Wadsworth, I. Zozoulenko, M. Berggren, E. Stavrinidou, S. Inal, I. McCulloch, *Adv. Mater.* **2020**, *32*, 2002748.

[41] D. A. Bernards, G. G. Malliaras, *Adv. Funct. Mater.* **2007**, *17*, 3538.

[42] V. A. Nguyen, C. Kuss, *J. Electrochem. Soc.* **2020**, *167*, 065501.

[43] F. Zou, A. Manthiram, *Adv. Energy Mater.* **2020**, *10*, 2002508.

[44] H. Chen, M. Ling, L. Hencz, H. Y. Ling, G. Li, Z. Lin, G. Liu, S. Zhang, *Chem. Rev.* **2018**, *118*, 8936.

[45] H. Zhao, Z. Wang, P. Lu, M. Jiang, F. Shi, X. Song, Z. Zheng, X. Zhou, Y. Fu, G. Abdelbast, X. Xiao, Z. Liu, V. S. Battaglia, K. Zaghib, G. Liu, *Nano Lett.* **2014**, *14*, 6704.

[46] A. Giovannitti, I. P. Maria, D. Hanifi, M. J. Donahue, D. Bryant, K. J. Barth, B. E. Makdah, A. Savva, D. Moia, M. Zetek, P. R. F. Barnes, O. G. Reid, S. Inal, G. Rumbles, G. G. Malliaras, J. Nelson, J. Rivnay, I. McCulloch, *Chem. Mater.* **2018**, *30*, 2945.

[47] T. Nicolini, J. Surgailis, A. Savva, A. D. Scaccabarozzi, R. Nakar, D. Thuau, G. Wantz, L. J. Richter, O. Dautel, G. Hadziioannou, N. Stingelin, *Adv. Mater.* **2021**, *33*, 2005723.

[48] S. J. Kwon, R. Giridharagopal, J. Neu, S. Kashani, S. E. Chen, R. J. Quezada, J. Guo, H. Ade, W. You, D. S. Ginger, *J. Phys. Chem. C* **2024**, *128*, 2748.

[49] B. V. Khau, L. R. Savagian, M. De Keersmaecker, M. A. Gonzalez, E. Reichmanis, *ACS Mater. Lett.* **2019**, *1*, 599.

[50] N. Siemons, D. Pearce, H. Yu, S. M. Tuladhar, G. S. LeCroy, R. Sheelamanthula, R. K. Hallani, A. Salleo, I. McCulloch, A. Giovannitti, J. M. Frost, *Proc. Natl. Acad. Sci. USA* **2023**, *120*, 2306272120.

[51] J. Guo, L. Q. Flagg, D. K. Tran, S. E. Chen, R. Li, N. B. Kolhe, R. Giridharagopal, S. A. Jenekhe, L. J. Richter, D. S. Ginger, *J. Am. Chem. Soc.* **2023**, *145*, 1866.

[52] L. G. Kaake, B. Gompf, S. Ludwigs, *Chem. Mater* **2023**, *35*, 4532.

[53] B. A. Miller-Chou, J. L. Koenig, *Prog. Polym. Sci.* **2003**, *28*, 1223.

[54] Y. Liu, F. Liu, H. W. Wang, D. Nordlund, Z. Sun, S. Ferdous, T. P. Russell, *ACS Appl. Mater. Interfaces* **2015**, *7*, 653.

[55] S. Sweetnam, K. R. Graham, G. O. Ngongang Ndjawa, T. Heumüller, J. A. Bartelt, T. M. Burke, W. Li, W. You, A. Amassian, M. D. McGehee, *J. Am. Chem. Soc.* **2014**, *136*, 14078.

[56] S. R. Jackson, R. L. Kingsford, G. W. Collins, C. G. Bischak, *Chem. Mater.* **2023**, *35*, 5392.

[57] S. R. Jackson, G. W. Collins, R. L. Kingsford, P. W. Martin, J. N. Keller, C. G. Bischak, *J. Mater. Chem. C* **2024**, *12*, 9804.

[58] L. Q. Flagg, C. G. Bischak, J. W. Onorato, R. B. Rashid, C. K. Luscombe, D. S. Ginger, *J. Am. Chem. Soc.* **2019**, *141*, 4345.

[59] A. Savva, C. Cendra, A. Giugni, B. Torre, J. Surgailis, D. Ohayon, A. Giovannitti, I. McCulloch, E. Di Fabrizio, A. Salleo, J. Rivnay, S. Inal, *Chem. Mater.* **2019**, *31*, 927.
[60] A. Savva, R. Hallani, C. Cendra, J. Surgailis, T. C. Hidalgo, S. Wustoni, R. Sheelamanthula, X. Chen, M. Kirkus, A. Giovannitti, A. Salleo, I. McCulloch, S. Inal, *Adv. Funct. Mater.* **2020**, *30*, 1907657.
[61] A. R. Hillman, *J. Solid State Electrochem.* **2011**, *15*, 1647.
[62] N. Shpigel, M. D. Levi, S. Sigalov, T. S. Mathis, Y. Gogotsi, D. Aurbach, *J. Am. Chem. Soc.* **2018**, *140*, 8910.
[63] M. D. Levi, G. Salitra, N. Levy, D. Aurbach, J. Maier, *Nat. Mater.* **2009**, *8*, 872.
[64] M. D. Levi, S. Sigalov, G. Salitra, R. Elazari, D. Aurbach, *J. Phys. Chem. Lett.* **2011**, *2*, 120.
[65] T. Liu, L. Lin, X. Bi, L. Tian, K. Yang, J. Liu, M. Li, Z. Chen, J. Lu, K. Amine, K. Xu, F. Pan, *Nat. Nanotechnol.* **2019**, *14*, 50.
[66] Y. Ji, Z.-W. Yin, Z. Yang, Y.-P. Deng, H. Chen, C. Lin, L. Yang, K. Yang, M. Zhang, Q. Xiao, J.-T. Li, Z. Chen, S.-G. Sun, F. Pan, *Chem. Soc. Rev.* **2021**, *50*, 10743.
[67] F. C. Spano, *J. Chem. Phys.* **2005**, *122*, 234701.
[68] D. T. Scholes, P. Y. Yee, J. R. Lindemuth, H. Kang, J. Onorato, R. Ghosh, C. K. Luscombe, F. C. Spano, S. H. Tolbert, B. J. Schwartz, *Adv. Funct. Mater.* **2017**, *27*, 1702654.
[69] T. J. Aubry, K. J. Winchell, C. Z. Salamat, V. M. Basile, J. R. Lindemuth, J. M. Stauber, J. C. Axtell, R. M. Kubena, M. D. Phan, M. J. Bird, A. M. Spokoyny, S. H. Tolbert, B. J. Schwartz, *Adv. Funct. Mater.* **2020**, *30*, 2001800.
[70] M. Skompska, A. Szkurłat, *Electrochim. Acta* **2001**, *46*, 4007.
[71] P. Cavassin, I. Holzer, D. Tsokkou, O. Bardagot, J. Réhault, N. Banerji, *Adv. Mater.* **2023**, *35*, 2300308.
[72] K. A. Mazzio, A. H. Rice, M. M. Durban, C. K. Luscumbe, *J. Phys. Chem. C* **2015**, *119*, 14911.
[73] Y. Wu, C. Z. Salamat, A. León Ruiz, A. F. Simafranca, N. Akmanşen-Kalayci, E. C. Wu, E. Doud, Z. Mehmedovic´, J. R. Lindemuth, M. D. Phan, A. M. Spokoyny, B. J. Schwartz, S. H. Tolbert, *Chem. Mater.* **2024**, *36*, 5552.
[74] A. Hamidi-Sakr, L. Biniek, J.-L. Bantignies, D. Maurin, L. Hermann, N. Leclerc, P. Lévêque, V. Vijayakumar, N. Zimmermannm, M. Brinkmann, *Adv. Funct. Mater.* **2017**, *27*, 1700173.
[75] P. Y. Yee, D. T. Scholes, B. J. Schwartz, S. H. Tolbert, *J. Phys. Chem. Lett.* **2019**, *10*, 4929.
[76] E. Lim, A. M. Glaudell, R. Miller, M. L Chabinyc, *Adv. Electron. Mater.* **2019**, *5*, 1800915.
[77] M. Lu-Díaz, M. Duhandžic´, S. Harrity, S. Samanta, Z. Akšamija, D. Venkataraman, *J. Phys. Chem. C* **2024**, *128*, 5996.
[78] M. V. Voinova, M. Jonson, B. Kasemo, *Biosens. Bioelectron.* **2002**, *17*, 835.
[79] N. Shpigel, M. D. Levi, S. Sigalov, L. Daikhin, D. Aurbach, *Acc. Chem. Res.* **2018**, *51*, 69.
[80] F. Lundin, L. Aguilera, H. W. Hansen, S. Lages, A. Labrador, K. Niss, B. Frick, A. Matic, *Phys. Chem. Chem. Phys.* **2021**, *23*, 13819.
[81] B. Zayat, P. Das, B. C. Thompson, S. R. Narayan, *J. Phys. Chem. C* **2021**, *125*, 7533.
[82] D. Neusser, C. Malacrida, M. Kern, Y. M. Gross, J. van Slageren, S. Ludwigs, *Chem. Mater.* **2020**, *32*, 6003.
[83] O. J. Korovyanko, R. Österbacka, X. M. Jiang, Z. V. Vardeny, R. A. J. Janssen, *Phys. Rev. B* **2001**, *64*, 235122.
[84] M. G. Voss, D. T. Scholes, J. R. Challa, B. J. Schwartz, *Faraday Discuss.* **2019**, *216*, 339.